

# DESIGN EVOLUTION AND PERFORMANCE CHARACTERIZATION OF THE GTX AIR-BREATHING LAUNCH VEHICLE INLET

J.R. DeBonis\*, C.J. Steffen Jr.\*, T. Rice†, and C.J. Trefny\*

\*NASA Glenn Research Center  
Cleveland, OH 44135

†The Johns Hopkins University  
Applied Physics Laboratory  
Laurel, MD 20723

## ABSTRACT

The design and analysis of a second version of the inlet for the GTX rocket-based combine-cycle launch vehicle is discussed. The previous design did not achieve its predicted performance levels due to excessive turning of low-momentum corner flows and local over-contraction due to asymmetric end-walls. This design attempts to remove these problems by reducing the spike half-angle to 10- from 12-degrees and by implementing true plane of symmetry end-walls. Axisymmetric Reynolds-Averaged Navier-Stokes simulations using both perfect gas and real gas, finite rate chemistry, assumptions were performed to aid in the design process and to create a comprehensive database of inlet performance. The inlet design, which operates over the entire air-breathing Mach number range from 0 to 12, and the performance database are presented. The performance database, for use in cycle analysis, includes predictions of mass capture, pressure recovery, throat Mach number, drag force, and heat load, for the entire Mach range. Results of the computations are compared with experimental data to validate the performance database.

## INTRODUCTION

NASA Glenn Research Center has undertaken a program to enable low cost access to space, by developing a highly reusable launch vehicle concept called GTX (figure 1) (formerly Trailblazer)<sup>1</sup>. This vehicle is powered by a Rocket-Based Combined-Cycle (RBCC) engine (figure 2), which is designed to operate efficiently from lift-off to orbit by integrating a rocket and ramjet<sup>2</sup>. The system combines the high thrust-to-weight/low specific impulse characteristics of the rocket with the high specific impulse/low thrust to weight characteristics of the ramjet. The engines are located in three semi-circular engine pods near the aft portion of the vehicle. The engine operates in air-breathing modes from lift-off to between Mach 10 and 12, at which point the air-breathing engine flow path is closed off, and the rocket is turned back on to carry the vehicle out of the atmosphere and into orbit.

A critical component of the RBCC engine is the inlet. This device must efficiently capture and compress the air over the entire air-breathing portion of the flight. The design and performance characterization using computational fluid dynamics (CFD) of a first generation inlet was reported previously<sup>3,4</sup>. The CFD analyses consisted of the solution of the axisymmetric form of the Reynolds-averaged Navier-Stokes (RANS) equations. A subsequent sub-scale test of this geometry in the NASA Glenn 1-ft. by 1-ft. supersonic wind tunnel<sup>5</sup> revealed that the inlet did not achieve the contraction ratios predicted by the CFD. At Mach 6 the maximum contraction ratio achieved was approximately half the predicted value of 16. Both the excessive turning of the low-momentum corner flows and the local over-contraction due to the asymmetric end-walls were identified as possible reasons for the discrepancy between the CFD predictions and the experiment. The simplifying assumption of an axisymmetric flowfield in the CFD analysis allows for fast turn-around necessary to characterize the inlet performance

"Approved for public release, distribution is unlimited." This is a preprint or reprint of a paper intended for presentation at a conference. Because changes may be made before formal publication, this is made available with the understanding that it will not be cited or reproduced without the permission of the author.

over the entire Mach range. However, this assumption prevented the prediction of the mechanisms that most likely limited the contraction ratio in the sub-scale wind tunnel tests.

There are three objectives of the current work. The first objective is to develop a second-generation inlet that improves on the performance of the first design. This will be accomplished by reducing the amount of flow turning in the inlet and by creating end-walls that are planes of symmetry. The second objective is to characterize the performance of this inlet, using CFD, to enable accurate cycle analysis of the GTX propulsion system. The third objective is to validate the performance database with experimental data.

## INLET DESIGN

The same design methodology used for the first generation inlet was repeated here for the new inlet. Several key constraints were changed, based on the results of the first wind tunnel test to improve inlet performance. The excessive turning of the low-momentum corner flows was remedied by reducing both the centerbody spike angle and the throat angle. The spike half-angle of the centerbody was reduced from 12-degrees to 10-degrees. The angle of the inlet throat relative to the propulsion system axis was reduced from 15-degrees to 12-degrees (figure 2.a.). An aft-facing step, corresponding to the step in the centerbody, was added to the cowl. The steps help isolate the forward portion of the inlet from back-pressure feeding forward through the subsonic portion of the boundary layer and provide locations for fuel injection. The steps are sized such that the area changes across the steps by a factor of 1.5. A  $0.25r_c$ -long constant area section to facilitate scramjet ignition is located aft of the step. The angle at the end of the centerbody is specified at 15-degrees. A flat section is located on the forward portion of the cowl to allow the inlet to be oversped (shock inside the lip) without increasing the amount of flow turning.

Isentropic inlet contours, for Mach 5.631 operation, were generated using a method of characteristics design code<sup>6</sup> based on the aforementioned constraints. Mach 5.631 is the condition at the inflow plane to the inlet corresponding to a Mach 6 freestream. This was chosen as the key point in the flight envelope. Beyond this point, the required inlet contraction ratio does not change appreciably with Mach number. Centerbody shock-on-lip was specified at this Mach number and the location of the shoulder on the centerbody was placed to cancel the reflected cowl shock. Beyond this Mach number, the shock angle does not change significantly with increased Mach number due to the hypersonic Mach number independence principle. Thus, the reflected shock will remain near the shoulder for all hypersonic Mach numbers.

Several perfect gas CFD analyses using the NPARC code were done on preliminary configurations. The CFD solutions were used to evaluate the designs and provide guidance in adjusting isentropic contours. Changes to these contours are as follows. The shoulder on the centerbody was moved forward along the spike surface by  $0.03704r_c$  to accommodate viscous effects. The discontinuity at the shoulder was then replaced by a radius equal to 1.5 cowl lip radii, tangent to both the upstream (spike) and downstream (isentropic contoured) surfaces. The radiused shoulder increases the range of Mach numbers around the design point for which the reflected cowl shock is canceled. Finally, the method of characteristics design set the throat angle on the centerbody surface to 12-degrees, but the cowl angle was somewhat higher, resulting in convergence at the throat. This cowl angle was reduced to 12-degrees to eliminate the throat convergence. The final inlet geometry is detailed in table 1.

There are four reference stations that are important for cycle analysis (figure 2). Station 0 is the freestream. Station 1 is located at the tip of the inlet spike. This is the inflow plane for the inlet and the conditions here represent the flow after it has been compressed by the vehicle forebody. Reference 3 reports these flow conditions as a function of freestream Mach number. Station 2 is the inlet throat and is used as the nominal location for the start of supersonic combustion. Station 3 is the rocket thruster exit, located in the aft end of the centerbody.

## CFD METHOD

The flowfield was assumed to be axisymmetric so that two-dimensional CFD could be used. This assumption is valid for a large majority of the inlet flow. Only the effects of the inlet sidewalls/end-walls would alter the two-dimensionality of the flowfield. This assumption significantly reduces both the number of grid points required to describe the geometry and the computational cost for a solution. The two-dimensional CFD yielded timely results for the inlet design process and enabled a large number of cases to be run for cycle analysis.

### GRID GENERATION

The inlet geometry is defined by a series of cubic splines and other simple geometric shapes. The spline data was used to create a series of points on the inlet surfaces that were read into the grid generator. The grid generation software used for this project was GRIDGEN<sup>7</sup>.

All grids were generated such that the first grid point away from a viscous wall was placed at an average inner variable distance,  $y^+$ , of 1. This distance was computed based on assumed average skin friction and flowfield values, and was subsequently checked for accuracy. It has been shown<sup>8</sup> that proper resolution of the boundary layer is not possible unless at least one grid point is within a  $y^+$  of 2.

The effect of grid resolution on solution accuracy was previously examined<sup>3,4,9</sup> and the results were used to size the current grids. Grid sizes varied between approximately 20,000 and 30,000 points depending on topology. Typical grids are shown in figure 3. The grids use a blocked structure with point-to-point matching at the block interfaces. For started supersonic cases, it was not necessary to model the area above the cowl lip because the flow in this region does not influence the region of interest and is not captured by the inlet. Thus, the grid above the cowl lip was not used for most of these cases to reduce computational time. One run using a full grid was necessary to compute the cowl drag.

### PERFECT GAS ANALYSIS

Perfect gas analyses were performed for freestream Mach numbers up to 6. The NPARC code<sup>10</sup> was used for the perfect gas analyses. NPARC solves the Reynolds averaged Navier-Stokes equations in strong conservation law form using the Beam-Warming approximate factorizations algorithm<sup>11</sup>. Spatial discretization is performed using a central difference scheme. Jameson style artificial dissipation<sup>12</sup> is added for stability and to smooth shock oscillations and odd-even grid point decoupling. The code uses a perfect gas equation of state. The code has several options for modeling turbulence varying from algebraic zero transport equations to one and two equation models. Both the Chien low Reynolds number  $k-\epsilon$ <sup>13</sup> and Wilcox's  $k-\omega$  models<sup>14</sup> were investigated previously<sup>3</sup>. It was found that the two-equation models produce very similar answers. All data reported from the NPARC code was generated using the  $k-\epsilon$  model. Adiabatic walls were specified for all Mach numbers and cooled walls were simulated at Mach 4, 5, and 6. To simulate the cooled walls a constant wall temperature was specified on the centerbody aft of the shoulder and on the entire internal cowl surface. Table 2 lists the Mach numbers and corresponding wall temperatures.

### REAL GAS ANALYSIS

The GASP code<sup>15</sup> was used for the real gas analyses. GASP is a commercially available code that is developed and sold by Aerosoft Inc. For this analysis the code solved the Reynolds averaged Navier-Stokes equations using a third-order accurate upwind scheme and Roe's flux difference splitting<sup>16</sup>. Time discretization was done by a two-factor alternating direction implicit (ADI) scheme. Van Albada limiters<sup>17</sup> were employed for stability in the presence of discontinuities. The chemical kinetics model of

Kang et. al.<sup>18</sup> was used. The equilibrium vibrational thermodynamics model was selected. The k- $\omega$  turbulence model was found most robust and was used for all GASP results herein. Results from the analysis of the previous configuration showed that the NPARC code using the k- $\epsilon$  turbulence model and the GASP code using the k- $\omega$  turbulence model were in excellent agreement for several perfect gas simulations. All real gas simulations were run using cooled walls (see table 2).

Performance data for the real gas analysis were obtained from Response Surface Modeling of the GASP code results. Details of this technique can be found in reference 9. A relatively dense full-factorial experiment design in two parameters; flight Mach number (M) and inlet contraction ratio (CR) was used. The primary response variable of this study was a regression model of inlet total pressure recovery. The experimental design space covered the expected range of practical inlet operations during scramjet mode. The freestream Mach number ranged from 6 to 12, while the inlet contraction ratio ranged from 8 to 16. A regression model was assembled from linear, quadratic and bi-linear (simple interaction) terms; all higher order terms and interactions are assumed to be zero.

### INLET PERFORMANCE ANALYSIS

Solutions were run for the entire range of air-breathing station 0 Mach numbers from 0.5 to 12. The corresponding conditions at station 1 were used as the inflow conditions to the computation and were obtained from the forebody flowfield analyses reported in reference 3. The inlet operates in four distinct modes, subsonic, external compression, started/subsonic combustion and started/supersonic combustion. For the subsonic cases and external compression cases the centerbody is fully extended ( $\Delta x/r_c = -0.98$ ) and the mass flux on the outflow boundary was regulated to control the inlet flow. Beyond the starting Mach number,  $M_0 > 2$ , the mass flux is regulated by the centerbody position. For the started subsonic combustion cases,  $2.5 \leq M_0 < 6$ , several supercritical (no imposed back-pressure) cases were run to determine the centerbody position that provided a practicable contraction ratio for engine operation. This contraction ratio provides adequate compression of the flow and a stable throat condition for back-pressuring the inlet. Then a back-pressure was imposed through the outflow boundary condition to simulate the effect of combustion process on the inlet flow. This back-pressure was increased in several increments until the inlet unstated. The data from the maximum back-pressure case is presented here. For the started supersonic combustion cases,  $M_0 \geq 6$ , only super-critical cases were necessary. For these cases, three contraction ratios, 8, 12, and 16 were analyzed.

Figure 4 plots the contraction ratios analyzed versus station 1 Mach number. Also plotted is the scheduled contraction ratio used in the GTX vehicle cycle analysis. At Mach 5.5 the engine operates in subsonic combustion mode and the inlet is contracted beyond the design contraction of 12. At Mach 6 the engine is transitioned to supersonic combustion by extending the centerbody, reducing the contraction ratio to 12. Transitioning from subsonic to supersonic combustion by moving the centerbody ensures symmetric thrust for the GTX vehicle. If the 3 engine pods were allowed to transition naturally, the transition for each engine may occur at different times. The throat (station 2) Mach numbers corresponding to the above contraction ratios are shown in figure 5.

Mach number contours representing three different station 0 Mach numbers are presented in figure 6. The Mach 0.8 solution is at a super-critical back-pressure. The flow chokes at the throat, located at the centerbody step, and then expands supersonically. Also, evident is a low-pressure region on the forward-facing portion of the cowl. This low-pressure results in a thrusting (suction) force for the vehicle. At Mach 2.0 the inlet operates in external compression mode. A classic lambda-shock pattern is seen just forward of the cowl lip. This creates a large flow separation that reduces the available flow area and an aerodynamic throat forms at the cowl lip. At Mach 5.0 the inlet is operating below the shock-on-lip Mach number and it captures 90 percent of the maximum possible airflow. The contours shown are from the maximum back-pressure case and they indicate that the steps in the cowl and centerbody effectively isolate the forward portion of the inlet (upstream of the throat) from the back-pressure.

Integrated one-dimensional performance data were computed from the two-dimensional solutions using a stream thrust averaging technique. Stream thrust averaging conserves mass, momentum and energy and provides a consistent set of data for cycle analysis. The details of the averaging technique are provided for a perfect gas in reference 3 and for a chemically reacting flow in reference 19. For the performance data presented, symbols are used to represent the results from the CFD analyses and solid lines are used to represent the curve fits used in cycle analysis.

## MASS CAPTURE

Inlet mass capture, expressed in terms of area ratio ( $A_1/A_c$ ) is plotted versus station 1 Mach number in figure 7. Subsonic, external compression, and started regions are denoted by different symbols. The inlet starts between Mach 2 and 2.5 and the shock-on-lip condition occurs at a freestream Mach number of 6. Real gas results are plotted for all 3 contraction ratios analyzed (8, 12, and 16). The discrepancy in the data at the shock-on-lip point ( $M_1=5.631$ ) is caused by the difference in spike position for each contraction ratio. For the subsonic and external compression cases the maximum airflows are shown. These were determined by specifying a low static pressure at the outflow boundary. Then several sub-critical cases were run by specifying a lower mass flux at the outflow boundary to determine the total pressure recovery and inlet drag as a function of airflow. A typical plot of pressure recovery and inlet drags versus mass capture is shown for Mach 0.5 in figure 8. Linear curve fits for the variation of recovery and inlet drags with mass flow ratio were developed for the vehicle cycle analysis.

## RECOVERY

Stream thrust averaged total pressure recovery is presented in figure 9. For the perfect gas solutions, isentropic perfect gas relations were applied to the stream thrust averaged pressure and Mach number to obtain the stagnation condition. The reference stagnation condition, at station 1, was also obtained from isentropic relations. For the real gas solutions, the equilibrium air stagnation condition was determined from the stream thrust averaged state using the Chemical Equilibrium Analysis code.<sup>20</sup> The stagnation condition of the reference state, station 1, was also calculated this way. Between Mach 4 and 6 the combustion process transitions between subsonic and supersonic combustion modes so recoveries at both stations 2 and 3 are presented. Both perfect gas and real gas station 2 recoveries are shown.

The effect of Reynolds number on inlet recovery was examined using the NPARC code. A Mach 6 adiabatic wall case was run at both vehicle scale and sub-scale Reynolds number. The sub-scale conditions were chosen to match those of the inlet test in NASA Glenn's 1-ft. by 1-ft. supersonic wind tunnel. The analysis indicates that the recovery is reduced by approximately 25 percent due to Reynolds number effects. This result is consistent with both the wind tunnel data and supporting three-dimensional CFD calculations<sup>21</sup>.

## INLET DRAG

In the GTX force accounting system, inlet drag is made up of two components, additive drag due to spillage and cowl drag. The additive drag is defined as the force exerted on the captured stream tube and is computed using a control volume technique outlined in reference 3. Figure 10 plots the additive drag versus station 1 Mach number. For the subsonic and external compression cases the additive drag varies inversely with the mass capture and it is at a maximum at transonic Mach numbers where the inlet mass capture is at a minimum. When the inlet starts, the normal shock located on the inlet spike is swallowed and the additive drag is significantly reduced. Beyond Mach 6, the shock-on-lip condition, no flow is spilled and the additive drag is zero. Cowl drag is defined as the force on the forward facing cowl surface and is computed by integrating the pressure and skin friction over this area. At low Mach numbers,  $M_1 < 1.5$ , the pressure on the cowl surface is lower than ambient and results in a thrust/suction

force which helps offset the high additive drag (figure 11). Beyond Mach 2, the cowl drag coefficient remains relatively constant.

### HEAT LOADS

For the cases run with cooled walls, the heat load up to station 2 was evaluated using a control volume analysis. The heat loads are plotted against station 0 Mach number in figure 12. The freestream Mach number is used because it is this condition which determines the total enthalpy of the flow. A linear curve fit of the data was used in the vehicle cycle analysis. The perfect gas results yield larger than expected heat loads because the perfect gas assumption does not allow energy transfer to the vibrational modes of the gas, resulting in high temperatures near the wall. The variation in heat load with contraction ratio was found to increase with Mach number.

### VALIDITY OF THE CFD DERIVED DATABASE

Sub-scale testing of the first inlet configuration revealed discrepancies between the axisymmetric CFD results and the experimental data. The effects of the end-walls, while localized, significantly reduced the achievable contraction ratios. Also, the lower Reynolds number of the sub-scale tests has been shown to reduce total pressure recovery. Results of sub-scale testing and supporting three-dimensional CFD analysis of the current configuration provide three important conclusions regarding the validity of the database<sup>21</sup>. First, the axisymmetric approximation is valid in the regions away from the end-wall. Second, the use of boundary-layer bleed on the end-walls significantly reduces the end-wall effects at the higher Mach numbers ( $M_1 > 3$ ). And finally, the Reynolds number effects significantly alter the inlet performance at the model scale.

To more closely validate the axisymmetric CFD derived database an axisymmetric sub-scale inlet model was built and tested at the Johns Hopkins University Applied Physics Laboratory. A 4 percent scale model was tested at a Mach 4, 22,000-ft. flight condition in the Applied Physics Lab's Cell 2 free jet facility<sup>22</sup> (figure 13). Results indicate that the mean maximum contraction ratio achieved was 10.32. Two CFD simulations were run which bracket the experimental maximum contraction ratio. A started solution was obtained at a CR of 9.19 and an unstarted solution was obtained at a CR of 12.0. Surface static pressures on the cowl and centerbody surfaces are compared in figure 14, for a contraction ratio of 8.696. The CFD results are in good agreement with the experimental data up to the inlet throat ( $x/r_c \approx -2.0$ ). The experimental data is super-critical and the CFD simulation was back-pressured. Hence, agreement aft of the inlet throat is not expected.

### CONCLUSIONS

A second version of the air-breathing inlet for the GTX rocket-based combine-cycle launch vehicle has been developed. This design improves on the first design by reducing the amount of turning of the low momentum flow on the end-walls and by implementing true plane of symmetry end-walls. The centerbody spike angle was reduced from 12- to 10-degrees and the angle the throat makes with the vehicle axis was reduced from 15- to 12-degrees. Axisymmetric Reynolds-Averaged Navier-Stokes simulations using both perfect gas and real gas, finite rate chemistry, assumptions were performed to aid in the design process and to create a comprehensive database of inlet performance. The inlet design, which operates over the entire air-breathing Mach number range from 0 to 12, and the performance database are presented. The performance database, for use in cycle analysis, includes predictions of mass capture, pressure recovery, throat Mach number, drag force, and heat load, for the entire Mach range. The database is validated with data from a sub-scale test of a fully axisymmetric configuration at Mach 4 flight conditions. Good agreement was found between the CFD and experiment.

## NOMENCLATURE

A	cross sectional area
CR	contraction ratio
D	drag
M	Mach number
Q	dynamic pressure
p	pressure
r	radius
x	distance from station 3
y <sup>+</sup>	inner variable distance from wall

## SUBSCRIPTS

0	station 0, freestream
1	station 1, inlet spike tip location
2	station 2, inlet throat
3	station 3, end of centerbody
arc	centerbody shoulder radius
c	capture
cl	cowl
cb	centerbody
t	total condition

## REFERENCES

1. Trefny, C.J., "An Air-Breathing Launch Vehicle Concept for Single-Stage-to-Orbit," AIAA Paper 99-2730, June 1999.
2. Escher, W.J.D., "Synerjet for Earth/Orbit Propulsion: Revisiting the 1966 NASA/Marquardt Composite (Airbreathing/Rocket) Propulsion System Study," SAE Paper 851163, May 1985.
3. DeBonis, J.R., Trefny, C.J., and Steffen Jr., C.J., "Inlet Development for a Rocket Based Combined Cycle, Single Stage to Orbit Vehicle Using Computational Fluid Dynamics," AIAA Paper 99-2239, NASA TM-1999-209279, June 1999.
4. Steffen Jr., C.J., and DeBonis, J.R., "Numerical Analysis of the Trailblazer Inlet Flowfield for Hypersonic Mach Numbers," AIAA 2000-0889, NASA TM-1999-209654, January 2000.
5. DeBonis, J.R. and Trefny, C.J., "Supersonic Wind Tunnel Tests of a Half-Axisymmetric 12°-Spike Inlet to a Rocket-Based Combined-Cycle Propulsion System," NASA TM-2001-210567, February 2001.
6. Anderson, B.H., "Design of Supersonic Inlets by a Computer Program Incorporation the Method of Characteristics," NASA TN D-4960, January 1969.
7. GridGen Version 13 Users Manual, Pointwise Inc., Bedford Texas, 1998.
8. Georgiadis, N.J., Dudek, J.C., and Tierney, T.P., "Grid Resolution and Turbulent Inflow Boundary Conditions Recommendations for NPARC Calculations," AIAA Paper 95-2613, July 1995.
9. Steffen Jr., C.J., "Response Surface Modeling of Combined-Cycle Propulsion Components Using Computational Fluid Dynamics," AIAA Paper 2002-0542, January, 2002.

10. Power, G.D., Cooper, G.K. and Sirbaugh, J.R., "NPARC 2.2 – Features and Capabilities," AIAA Paper 95-2609, July 1995.
11. Beam, R. and Warming, R.F., "An Implicit Finite Difference Algorithm for Hyperbolic Systems in Conservation Law Form," Journal of Computational Physics, vol. 22, no. 1, September 1976.
12. Jameson, A., Schmidt, W., and Turkel, E., "Numerical Solutions of the Euler Equations by Finite Volume Methods using Runge-Kutta Time Stepping Techniques," AIAA Paper 81-1259, June 1981.
13. Chien, K.-Y., "Predictions of Channel and Boundary-Layer Flows with a Low-Reynolds-Number Turbulence Model," AIAA Journal, vol. 20, no. 1, pp.33-38.
14. Wilcox, D.C., Turbulence Modeling for CFD, DCW Industries, Inc. La Canada, CA, 1993.
15. General Aerodynamic Simulation Program Version 3: User Manual, ISBN 0-9652780-0-X, Aerosoft Inc., Blacksburg, Virginia, 1996.
16. Roe, P.L. "Approximate Riemann Solvers, Parameter Vectors and Difference Schemes," Journal of Computational Physics, vol. 43, pp. 357-372, October 1981.
17. Van Albada, G.D., Van Leer, B., and Roberts, W.W., "A Comparative Study of Computational Methods in Cosmic Gas Dynamics," Astronomy and Astrophysics, vol. 108, no. 1, pp. 76-84, April 1982.
18. Kang, S.-W., Dunn, M.G., and Jones, W.L., "Theoretical and Measured Electron Density distributions for the RAM Vehicle at High Altitudes," AIAA Paper 72-689, June 1972.
19. Riggins, D.W. and McClinton, C.R., "Analysis of Losses in Supersonic Mixing and Reacting Flows," AIAA Paper 91-2266, June 1991.
20. Gordon, S. and McBride, B.J., "Computer Program for Calculation of Complex Chemical Equilibrium Compositions and Applications; Part I, Analysis," NASA Reference Publication 1311, October 1994.
21. Frate, F.C., and Slater, J.W., "Supersonic Wind Tunnel Tests of an Axisymmetric Sector, 10°-Spike Inlet to a Rocket-Based Combined-Cycle Propulsion System," Proceedings of the JANNAF 26th Airbreathing Propulsion Subcommittee Meeting, Destin, Florida, April 2002.
22. Van Wie, D.M., Thompson, M.W., D'Alessio, S.M., and Grossman, K.R., "Refurbishment of the JHU/APL Hypersonic Airbreathing Engine Test Facilities," AIAA Paper 2000-2645, June 2000.



	$x_{cl}/r_c$	$r_{cl}/r_c$	A	B	C	D
Cowl lip	-3.7401	1.00000				
Begin 1 <sup>st</sup> cowl spline	-3.3401	1.00000	2.2781E-02	1.0343E-01	-7.1482E-02	4.5619E-01
Begin 2 <sup>nd</sup> cowl spline	-1.9865	0.84105	-6.4626E-04	5.1574E-02	1.2129E-09	6.3246E-01
Station 3	0.0000	0.63246				

a. Cowl

	$x_{cb}/r_c$	$r_{cb}/r_c$				
Spike tip	-7.1988	0.00000				
Begin circular arc	-2.5650	0.81707	$r_{arc}/r_c$ 1.50000	$x_{arc}/r_c$ -2.64410	$y_{arc}/r_c$ -0.66014	D
Begin 1 <sup>st</sup> c.b. spline	-2.3092	0.83985	A	B	C	D
Begin 2 <sup>nd</sup> c.b. spline	-1.6631	0.76491	-4.1639E-02	-4.5657E-01	-1.5392E+00	-8.0758E-01
Begin 3 <sup>rd</sup> c.b. spline	-1.4142	0.70992	-1.7876E-01	-1.0633E+00	-2.3207E+00	-1.0538E+00
Centerbody trailing edge	0.0000	0.27555	5.2938E-02	1.5651E-01	-1.7996E-01	1.9846E-01

b. Centerbody

Splines defined by,  $\frac{r}{r_c} = A \left( \frac{x}{r_c} \right)^3 + B \left( \frac{x}{r_c} \right)^2 + C \frac{x}{r_c} + D$

Table 1. Inlet geometry

$M_0$	$T_w (^\circ R)$
4	500
5	500
6	900
9	1200
12	1500

Table 2. Isothermal wall temperatures

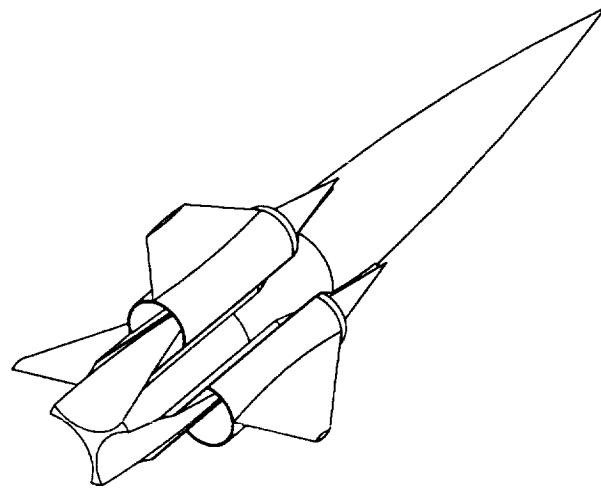
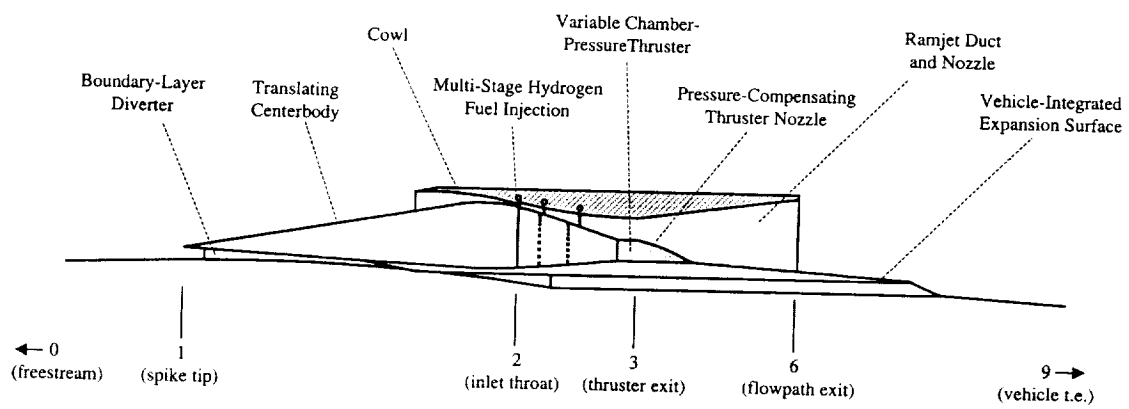
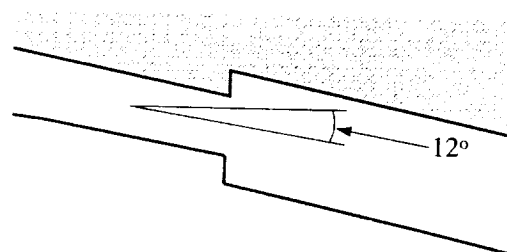


Figure 1. GTX vehicle

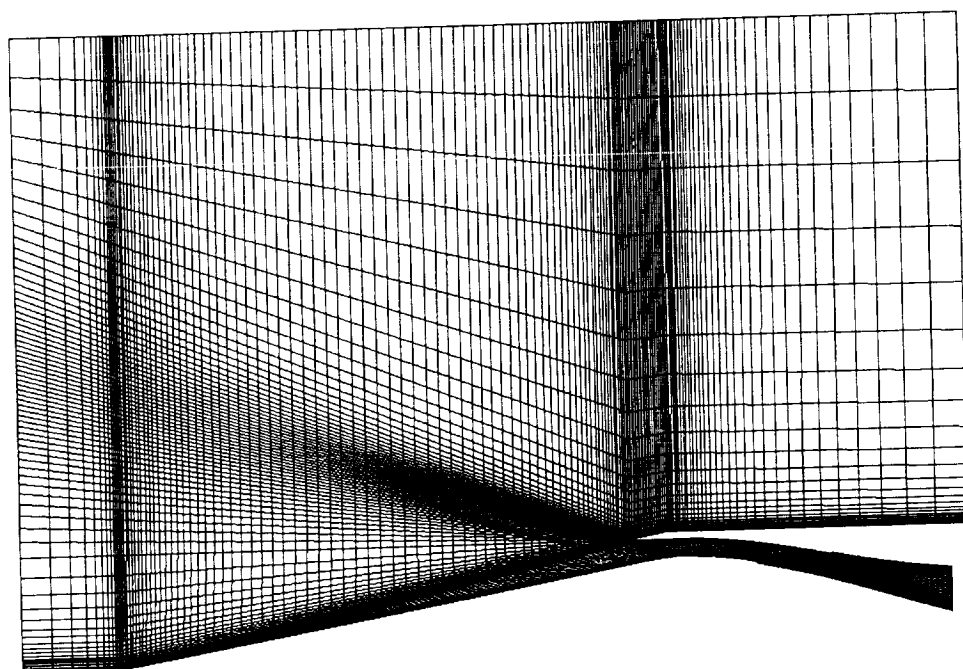


a. Entire engine

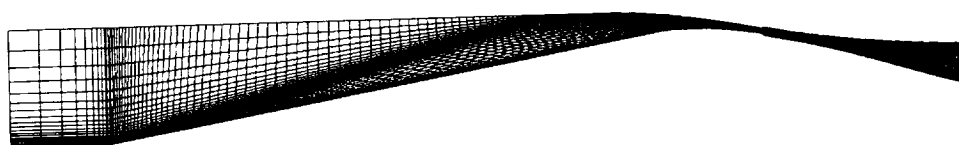


b. Detail of inlet throat

Figure 2. Engine schematic



a. Full grid



b. Reduced grid for started supersonic cases

Figure 3. Computational grid

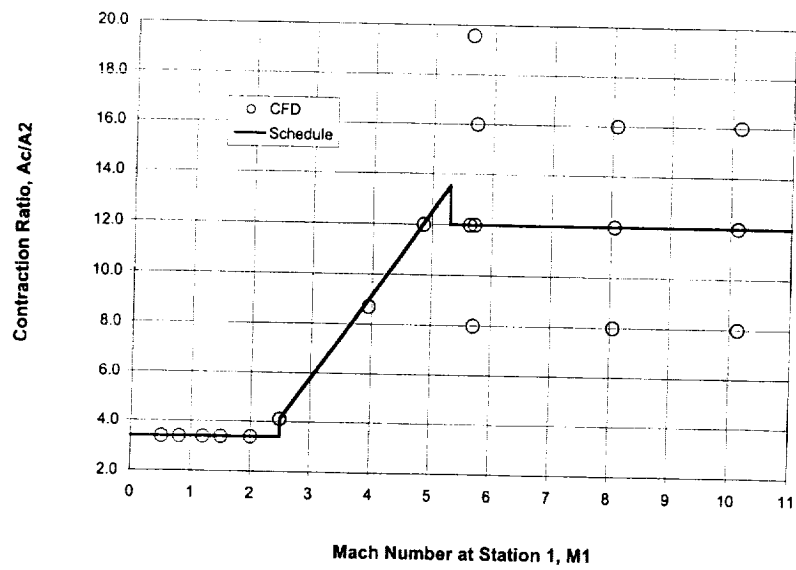


Figure 4. Contraction Ratio

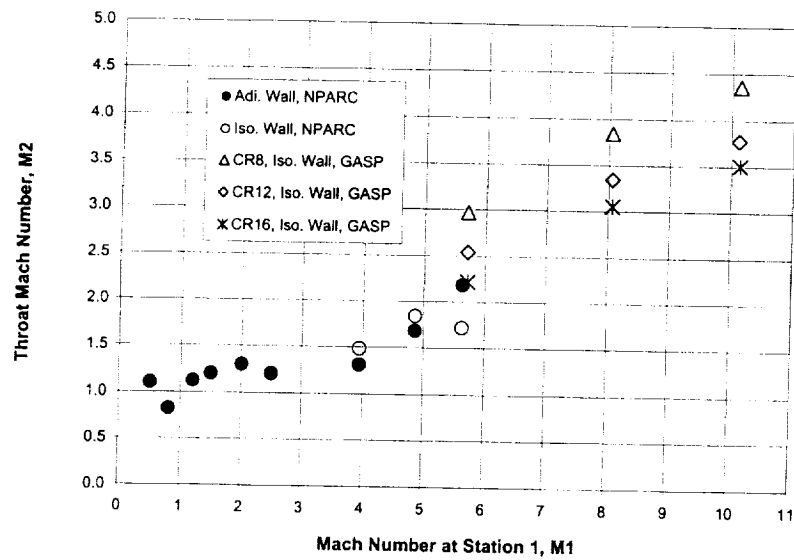
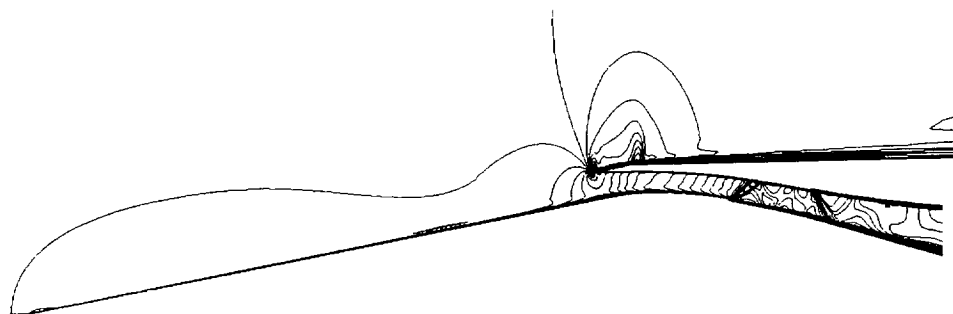
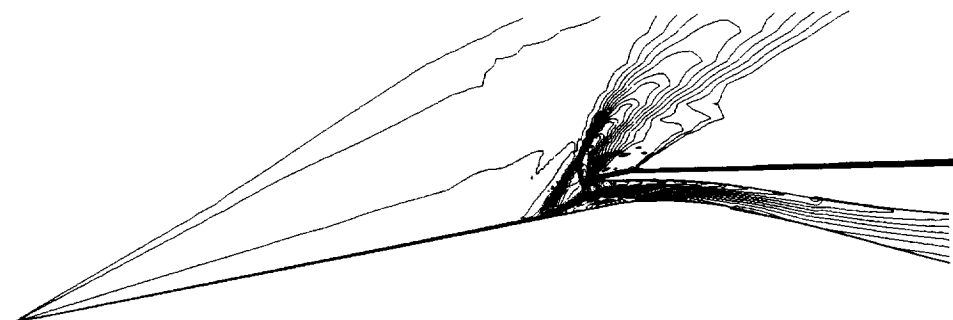


Figure 5. Throat Mach number



a. Mach 0.8



b. Mach 2.0



c. Mach 5.0

Figure 6. Mach number contours

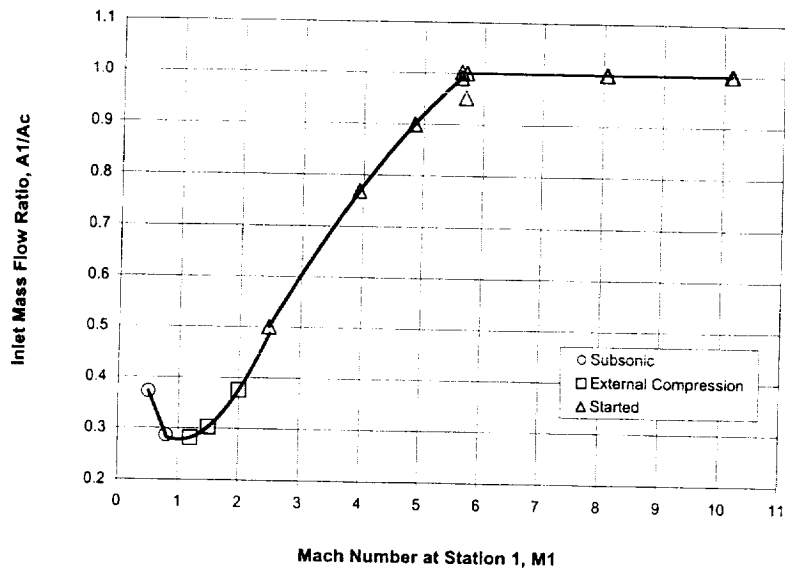


Figure 7. Inlet mass capture

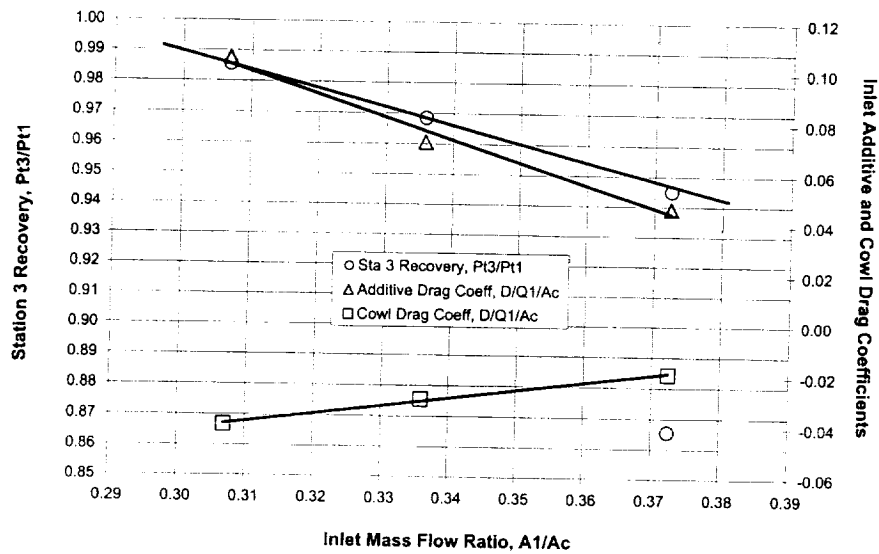


Figure 8. Total pressure recovery and inlet drag as a function of mass capture at  $M_0 = 0.5$

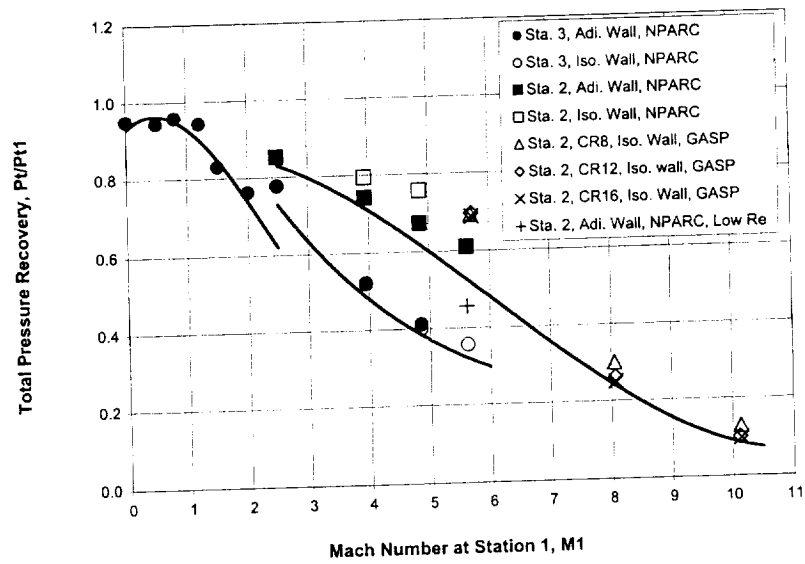


Figure 9. Inlet recovery

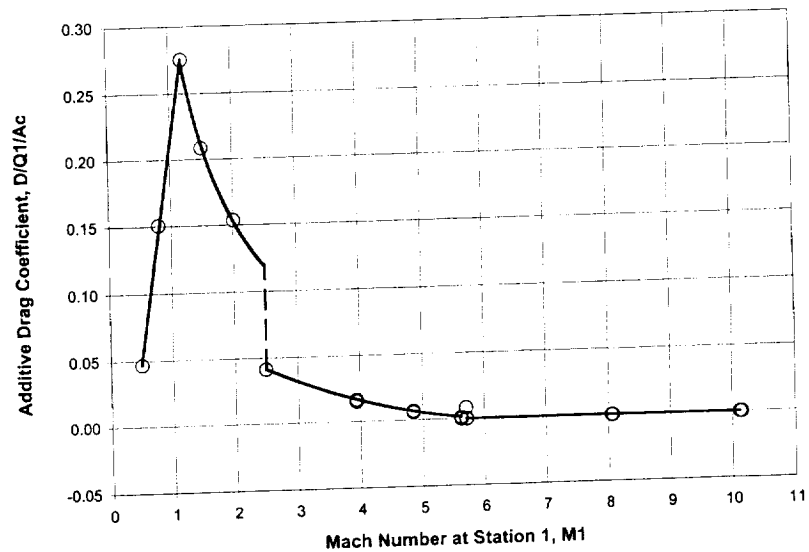


Figure 10. Additive Drag

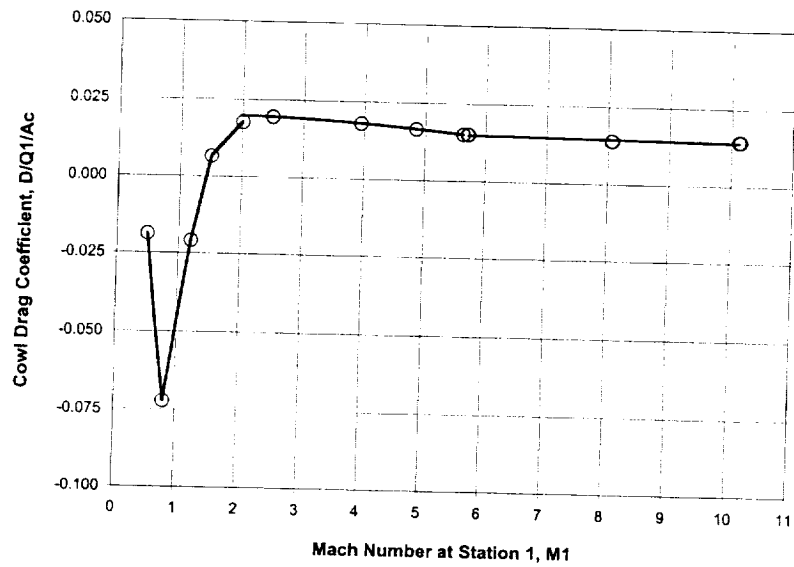


Figure 11. Cowl drag

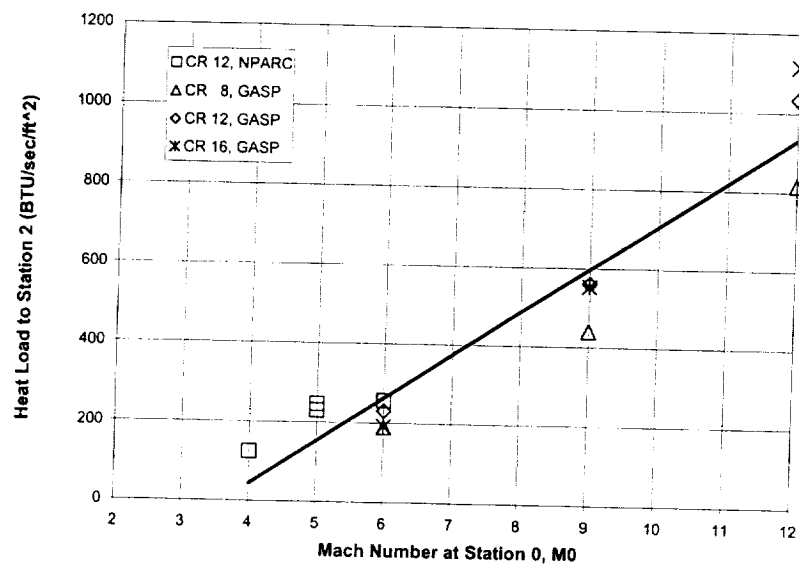


Figure 12. Heat loads



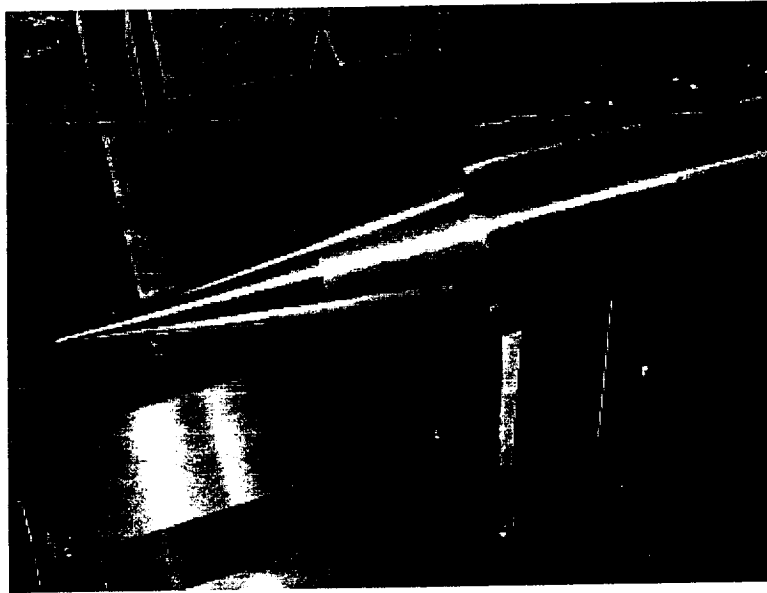


Figure 13. Sub-scale inlet model in APL facility

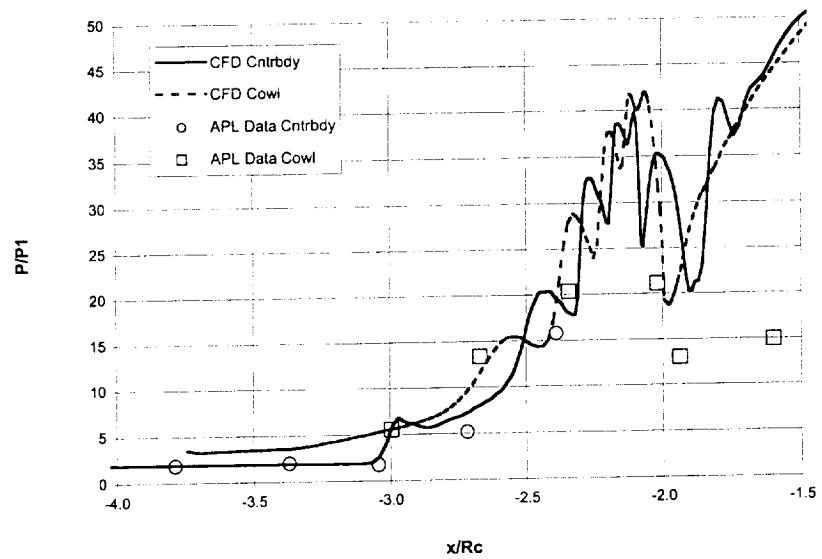


Figure 14. Comparison of CFD to APL experiment

